PAPER

Check for updates

Novel aqueous amine looping approach for the direct capture, conversion and storage of CO_2 to produce magnesium carbonate†

Meishen Liu,[a] Hassnain Asgar,[a] Soenke Seifert[b] and Greeshma Gadikota*[a]

Designing novel integrated chemical pathways for the capture, conversion, and storage of CO_2 is a crucial need for advancing sustainable energy conversion. The accelerated conversion of CO_2 to water-insoluble and stable magnesium carbonate is a thermodynamically downhill route for permanently storing CO_2. However, a practical constraint of carbon mineralization is the slow kinetics at low CO_2 concentrations. In this study, we investigate a direct integrated mineralization approach, whereby CO_2, amine solvents (such as monoethanolamine, MEA), water and alkaline Mg-bearing solids are reacted in a slurry reaction environment. About 70% conversion of magnesium oxide to magnesium carbonate was achieved at 50 °C after 3 hours. The looping of amine-bearing solvents between the CO_2 loaded and release states, facilitates the accelerated conversion of magnesium-bearing oxides to magnesium carbonate. Hydrated magnesium carbonate and magnesium hydroxide phases were noted when less than complete conversion of magnesium oxide was achieved. The morphological features were determined using *in operando* ultra-small and small angle X-ray scattering (USAXS/SAXS) and grazing incidence-small angle X-ray scattering (GI-SAXS) measurements. The proposed pathway is an adaptive, low temperature, single-step approach for the direct capture, conversion and storage of CO_2. By demonstrating the effectiveness of aqueous alkaline amine looping approach for the accelerated carbon mineralization of MgO, we aim to expand this approach to include heterogeneous alkaline industrial residues such as coal fly ash and steel slag and naturally occurring minerals such as magnesium silicate and calcium silicate.

1. Introduction

Rising anthropogenic carbon emissions to the atmosphere to the order of 35 000 million metric tons of CO_2 and the heterogeneity in gaseous waste streams call for the development of adaptive and transformative technologies for integrated CO_2 capture, utilization and storage.[1] Carbon mineralization which involves converting CO_2 to water insoluble and stable Ca- and Mg-carbonates is a thermodynamically downhill pathway for the integrated capture, utilization and storage of CO_2.[1–17] Ca- and Mg-bearing alkaline feedstocks include earth abundant silicate-rich minerals such as olivine ($(Mg, Fe)_2SiO_4$), wollastonite ($CaSiO_3$), and serpentine ($(Mg, Fe)_3Si_2O_5(OH)_4$), and alkaline industrial residues such as coal fly ash, steel slag, cement kiln dust, and red mud.[18–21]

Broadly, two main approaches have been developed for the accelerated conversion of CO_2 to Ca- and Mg-carbonates. In the first approach, high purity silica and carbonates are produced through the sequential use of acids and bases. Acids are used for extracting Ca and Mg ions into the aqueous phase with concurrent production of silica. Bases are then used to increase pH and enhance the generation of carbonate ions for producing Ca- and Mg-carbonates.[7,8,15,22–24] This approach facilitates the production of high purity silica and Ca- and Mg-carbonates. Another approach involves using elevated temperatures greater than 90 °C and high CO_2 pressures greater than 50 atm to accelerate carbon mineralization.[4,12,15] Several rate limiting steps such as CO_2 hydration, mineral dissolution and carbonate precipitation are overcome at these experimental conditions. For example, elevated CO_2 pressures enable enhanced CO_2 solvation in the aqueous phase.[25,26] Elevated temperatures accelerate dissolution of Ca- and Mg-bearing silicate minerals.[27–31] The solubility of Ca- and Mg-carbonates decreases with increasing temperature which aids the precipitation of Ca- and Mg-carbonates.[32–34]

The motivation for exploring low temperature hydrothermal routes for enhanced carbon mineralization emerges from the high temperature and pressure associated with direct gas–solid reaction routes. Complete conversion of $Mg(OH)_2$ to

[a]*School of Civil and Environmental Engineering, Cornell University, 527 College Avenue, 117 Hollister Hall, Ithaca, NY 14850, USA. E-mail: gg464@cornell.edu; Tel: +1 609-255-4796*

[b]*X-Ray Science Division, Advanced Photon Source, Argonne National Laboratory, Building 433A, 9700 Cass Avenue, Lemont, IL 60439, USA*

† Electronic supplementary information (ESI) available. See DOI: 10.1039/c9se00316a

magnesium carbonate is achieved at reaction temperature of 500 °C and CO_2 partial pressure of 340 bar in less than two hours.[5] About 30% conversion of serpentine to magnesium carbonate is achieved at 340 bar and temperatures in the range of 140 to 300 °C.[5] In comparison, hydrothermal pathways reported by Gerdemann and co-workers[4] and Gadikota and co-workers[11] show that about 80% or higher conversion of olivine bearing 47.3 wt% MgO is converted to $MgCO_3$ at experimental conditions of 185 °C, 1.0 M NaCl + 0.64 M $NaHCO_3$, 15 wt% solid, pCO$_2$ of 150 atm[4] or 139 atm[11] at reaction times of 5 hours or greater. As reported by Gerdemann and co-workers,[4] these high temperatures and CO_2 partial pressure requirements contribute to the high energy needs for carbon mineralization.

Efforts to accelerate carbon mineralization at lower temperatures and using flue gas streams led to the exploration of pathways to decouple CO_2 solubility, mineral dissolution and carbonate precipitation steps. To overcome the challenge of low solubility of CO_2 in water, additives such as carbonic anhydrase have been proposed.[35–37] The use of organic ligands such as oxalate, citrate or acetate were proposed to enhance mineral dissolution.[38,39] Seeding surfaces of calcite and magnesite were found to aid the accelerated precipitation of the same phases.[40,41] However, these accelerated pathways were developed independently, without considering their intended influence on coupling multiple reactions for accelerated carbon mineralization. Therefore, the scientific challenge lies in accelerating "step change" advancements in carbon mineralization. This is achieved by synergistically coupling multiple reaction pathways to direct the synthesis of Ca- and Mg-carbonates at temperatures below 100 °C using dilute flue gas streams of CO_2.

In this study, we evaluate the hypothesis that utilizing aqueous amine-bearing solvents such as monoethanolamine (MEA) enhances CO_2 hydration *via* the enhanced formation of bicarbonate and carbonate species in the aqueous phase at relatively low temperature and low pressure. Carbonate and bicarbonate ions then react with dissolved Ca and Mg in the aqueous phase to produce Ca- and Mg-carbonates. Fig. 1 is a schematic representation of the proposed mechanism. The integrated gas–liquid–solid reaction pathways shown in Fig. 1 represent the coupling of multiple reactions including enhanced CO_2 capture and hydration using MEA solvents, mineral dissolution and carbonate precipitation. Alternatively, CO_2-loaded amine-bearing solutions can be directly reacted with oxides, hydroxides or silicates of Ca and Mg in a slurry reaction environment to produce Ca- and Mg-carbonates. Both pathways involve the looping of the amine-bearing solvents from the CO_2-loaded to CO_2-release states by converting CO_2 to Ca- and Mg-carbonates. This novel aqueous alkaline amine looping process was successfully demonstrated for the accelerated mineralization of calcium oxide and calcium chloride to produce calcium carbonate.[9,42,43] Carbonate-induced

Dilute CO₂ bearing waste gas streams

CO₂ Hydration

$$CO_{2(g)} + H_2O \longleftrightarrow H_2CO_{3(aq)}$$
$$H_2CO_{3(aq)} \longleftrightarrow H^+_{(aq)} + HCO_3^-_{(aq)}$$
$$HCO_3^-_{(aq)} \longleftrightarrow H^+_{(aq)} + CO_3^{2-}_{(aq)}$$

CO₂ Capture by Amine

$$CO_{2(g)} + RNH_{2(aq)} \longleftrightarrow RNH_2^+COO^-_{(aq)}$$
$$RNH_2COO^-_{(aq)} + RNH_{2(aq)} \longleftrightarrow RNH_3^+_{(aq)} + RNHCOO^-_{(aq)}$$

Amine Regeneration

$$OH^-_{(aq)} + RNH_3^+/RR'NH_2^+_{(aq)} \longleftrightarrow RNH_2/RR'NH_{(aq)} + H_2O_{(l)}$$
$$H_2O_{(l)} + RNHCOO^-_{(aq)} \longleftrightarrow RNH_{2(aq)} + HCO_3^-_{(aq)}$$
$$H_2O_{(l)} + RR'NCOO^-_{(aq)} \longleftrightarrow RR'NH_{(aq)} + HCO_3^-_{(aq)}$$
$$HCO_3^-_{(aq)} \longleftrightarrow H^+_{(aq)} + CO_3^{2-}_{(aq)}$$

Cation Recovery from Ca- and Mg-bearing solids

$$MgO_{(s)} + H_2O_{(aq)} \longleftrightarrow Mg(OH)_{2(aq)} \longleftrightarrow Mg^{2+}_{(aq)} + 2OH^-_{(aq)}$$

Carbonate Formation

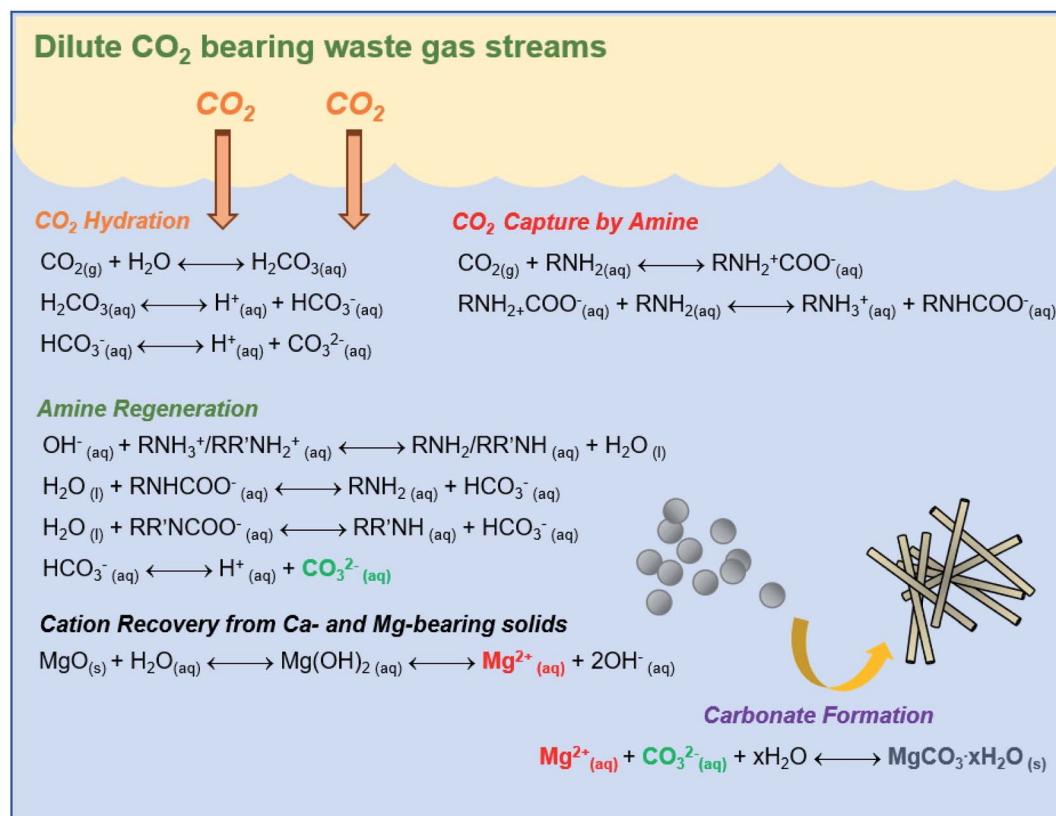$$Mg^{2+}_{(aq)} + CO_3^{2-}_{(aq)} + xH_2O \longleftrightarrow MgCO_3 \cdot xH_2O_{(s)}$$

Fig. 1 Schematic representation of the alkaline aqueous amine looping process for the carbon mineralization of magnesium oxide to produce magnesium carbonate.

solidification of calcium silicate using MEA was extensively studied.[18,44,45]

However, the carbon mineralization of Mg-bearing oxides, hydroxides or silicates using aqueous alkaline amine looping approach has not been established. Given the abundance of Mg-bearing minerals around the world, evaluating the reactivity of Mg-bearing minerals to produce Mg-bearing carbonates using the aqueous alkaline amine looping approach needs to be explored.[46,47] The successful demonstration of the proposed process will allow us to unlock the potential of vast resources of Mg-bearing minerals for the accelerated capture, conversion and storage of CO_2 in a single step. The aim of this study is to explore the feasibility of using Mg-bearing materials using simple precursors such as magnesium oxide for the accelerated capture, conversion and storage of CO_2 to produce magnesium carbonates. To achieve this aim, several research questions need to be addressed: (i) what is the influence of reaction temperature and MEA composition on the extent of carbon mineralization of magnesium oxide? (ii) What is the chemical composition of the carbonate-bearing materials? (3) How do the structural and morphological features of MgO dynamically evolve in these fluidic environments?

To address these research questions, laboratory-scale experiments were designed to probe the sensitivity of carbon mineralization behavior on the reaction conditions such as temperature and the composition of the MEA. This gas–liquid–solid reaction environment was designed for a constant pressure of 1 atm. The influence of aqueous phase compositions of 10–50 wt% MEA at temperatures in the range of 25–90 °C on the carbon mineralization behavior of MgO was probed. A slurry composition of 15 wt% solid was held constant for all the experiments. Continuous stirring at the rate of 300 rpm ± 5 rpm was maintained to reduce mass transfer limitations. A second of experiments were designed to probe dynamic time-resolved structural and microstructural evolution of magnesium oxide as it is reacted to produce magnesium carbonate using Ultra Small/Small/Wide Angle X-ray Scattering (USAXS/SAXS/WAXS) measurements.[2,10,14,48–51] Further, Grazing Incidence-Small Angle X-ray Scattering (GI-SAXS) measurements were performed to determine the size of the nucleating magnesium carbonate particles on silica interfaces. This comprehensive research approach was used to evaluate the effectiveness of the coupled reaction pathways in directing the synthesis of magnesium carbonates in multiphase reaction environments and the underlying structural and morphological basis for the observed reactivity.

2. Experimental materials and methods

Magnesium oxide used in this integrated carbon mineralization approach with aqueous alkaline amine looping approach was procured from Sigma-Aldrich. The mean particle size, surface area, and cumulative pore volume of magnesium oxide are 8.54 μm, 3.59 m^2 g^{-1}, and 0.0078 cm^3 g^{-1}, respectively. Monoethanolamine (MEA) with a purity of 98% used in these studies was procured from Alfa Aesar.

2.1 Aqueous alkaline amine looping process for accelerated carbon mineralization

The experiments to evaluate the influence of temperature and MEA concentrations on the accelerated conversion of magnesium oxide to magnesium carbonate using the aqueous alkaline amine looping process were performed in a batch environment (Parr Reactor, Series 4590 Micro Stirred Reactor). The slurry environment comprised 17 g of liquid and 3 g of solid sample. Aqueous phase compositions comprising deionized water, 10, 30, and 50 wt% MEA were used. CO_2 partial pressure of 1 atm was maintained throughout the length of the experiments. A constant stirring rate of 300 rpm ± 5 rpm was applied. Each experiment was performed over a length of 3 hours. Extents of carbon mineralization at reaction temperatures of 25 °C, 50 °C, 75 °C and 90 °C were evaluated. About 5–10 minutes were needed to reach the desired reaction temperature, which marked the beginning of the experiment. All experiments were performed over 3 hours. At the end of 3 hours, vacuum filtration was used to separate the liquid contents from the solids. The recovered solid was dried in a vacuum oven for 24 hours at 90 °C to remove any residual water in the solid sample.

2.2 Characterization of chemical and morphological properties

The carbon mineralization efficiency using the aqueous alkaline amine looping process was evaluated based on the extent of magnesium mineralized to produce magnesium carbonate. The carbonate content used in these calculations was determined using Thermogravimetric Analyses (TGA, TGA 550, TA Instruments). TGA data provides quantitative information into the changes in the weight of the samples on heating at specific temperatures. The heating rate was set to 5 °C min^{-1} from 25 °C to 800 °C and the flow rate of the N_2 gas was 25 mL min^{-1}. The carbonate content in nesquehonite was determined from the weight change in the temperature range of 350–450 °C.[52] The stoichiometric mass of MgO needed for storing a unit mass of CO_2 was defined as R_{CO_2}.[53,54] As reported in previous studies, the extent of carbon mineralization, $Y_{CO_2,TGA}$, a measure of the ratio of the amount of CO_2 present in the sample with respect to the CO_2 storage capacity was determined by the following relationship: $Y_{CO_2,TGA} = R_{CO_2} \times \left(\dfrac{TGA}{100 - TGA} \right) \times 100\%$ where TGA represents the weight change that corresponds to the carbonate content in the reacted materials. To identify the species in the aqueous and solid phases, Attenuated Total Reflection-Fourier Transform Infrared spectroscopy analyses were performed (ATR-FTIR, Thermo Fisher Nicolet iS 10). The spectra were collected in the range of 650–4000 cm^{-1}. The morphological features of the products were determined using Scanning Electron Microscopy (SEM, Hitachi High Technologies America, Hitachi S3400-N). The changes in the porosity and specific surface area of the powders were determined using the Brunauer–Emmett–Teller technique (BET, Quantachrome NOVAtouch® Analyzer, Boynton Beach, FL).

Time-resolved structural and microstructural features as MgO is reacted in the aqueous amine looping process were

determined using *in operando* Ultra Small/Small/Wide Angle X-ray Scattering (USAXS/SAXS/WAXS) measurements at Sector 9-ID at the Advanced Photon Source (APS) in Argonne National Laboratory (ANL).[2,3,10,14,48,51,55] The arrangement comprised of a cell with a continuous flow of CO_2 at the rate of 10 mL min^{-1}. In this *in situ* measurement, 1 mL 30 wt% CO_2-loaded MEA and 0.15 g MgO were added to an NMR tube with an internal diameter of 4 mm. CO_2 was continuously supplied to the aqueous phase to ensure high concentrations of inorganic carbon in the aqueous phase. The acquisition times for USAXS, SAXS, and WAXS were 90 s, 20 s, and 30 s respectively. Silver behenate was used to calibrate SAXS and LaB6 was used to calibrate WAXS measurements.[56] The total X-ray flux, energy and corresponding wavelength were 10^{-13} photon s^{-1}, 21.0 keV, and 0.59 Å, respectively. Irena[57] and Nika[58] software packages embedded in *IgorPro* (Wavemetrics, Lake Oswego, OR) were used for data analyses.[57,59] To capture the hierarchical morphological features during the carbonation of MgO, the combined USAXS/SAXS data were modeled using the "Modeling II" tool in Irena package.[57]

In situ Grazing Incidence-Small Angle X-ray Scattering (GI-SAXS) measurements were performed to determine the sizes of the nucleating particles. These measurements were conducted at the beamline 12 ID-B at the Advanced Photon Source (Argonne National Laboratory, USA). A custom designed cell was used for these measurements. The internal dimensions of this cell are 10 mm × 10 mm × 15 mm. 30 wt% CO_2-loaded MEA solution with a volume of 0.1988 mL was injected into 5 mL of 0.1 M $Mg(NO_3)_2$ solution, which marked the beginning of the *in situ* measurement. The X-ray beam was directed to the substrate with an incidence angle of $\alpha_i = 0.11°$ through the two Kapton windows. This incident angle is lower than the critical angle for total reflection (α_c-quartz = 0.14° at 14 keV incident X-ray energy). The scattered intensity from the nucleated magnesium carbonate particles was collected using a 2-dimensional Pilatus 2 M detector (Dectris Ltd., Baden, Switzerland). The incidence X-ray energy, a sample-to-detector distance (d_{s-d}), and q-range for these measurements were 14 keV, 2060 mm, and 0.005 Å^{-1} to 0.6 Å^{-1}, respectively. After background subtraction and 2D data reduction, the reduced data was fitted by Guinier–Porod fit[60] as shown in Fig. 7(c). The equations that describe the relationships of the generalized Guinier Law are listed below.[60]

$$I(Q) = \frac{G}{Q_s} \exp\left(\frac{-Q^2 R_g{}^2}{3-s}\right) \quad \text{for } Q \leq Q_1 \tag{1}$$

$$I(Q) = \frac{D}{Q^d} \quad Q \geq Q_1 \tag{2}$$

$$Q_1 = \frac{1}{R_g}\left(\frac{3d}{2}\right)^{1/2} \tag{3}$$

$$D = G \exp\left(\frac{-Q^2 R_g{}^2}{3}\right) Q_1{}^d = G \exp\left(\frac{-d}{2}\right)\left(\frac{3d}{2}\right)^{\frac{d}{2}} \frac{1}{R_g{}^d} \tag{4}$$

G and D are the Guinier and Porod scale factors. Q is the scattering variable, $I(Q)$ is the scattered intensity, R_g is the radius of gyration, d is the Porod exponent. Q_1 is set up to ensure the continuity of the slopes (derivatives). A dimensionality parameter $(3 - s)$ is defined to provide more flexibility for modeling different shapes of objects. For example, objects with spherical, rod-like, and lamellae or platelet dimensions, $s = 0, 1;$ or 2, respectively.[60] The R_g and Porod scale factors are calculated based on the equations represented above.

3. Results and discussion

3.1 Effect of temperature and MEA concentration

To evaluate the influence of temperature and MEA concentration on the extent of carbon mineralization of MgO, multiphase reaction environments are constructed. The pressure of CO_2 in the gas phase is held at 1 atm over the course of the experiment. The slurry was composed of 15 wt% solid. MEA compositions were evaluated as 10, 20, 30 and 50 wt% at temperatures of 25 °C, 50 °C, 75 °C, and 90 °C. Reaction times were set to 3 hours and the stirring rates at 300 rpm ± 5 rpm. The extents of carbon mineralization of MgO as a function of MEA concentration and temperature are noted in Fig. 2 and summarized in Table S1.† A non-linear relationship of the influence of temperature and MEA on the carbon mineralization of MgO was noted. The highest conversion of MgO to magnesium carbonate achieved with 30 wt% MEA at 50 °C is 70%. Subsequent increase in reaction temperature resulted in a lower extent of carbon mineralization. This is a result of the competing effects of temperature on CO_2 absorption and carbon mineralization. Temperatures below 50 °C favor CO_2 absorption in MEA[61] but the kinetics of carbon mineralization are slow. Higher temperatures favor carbon mineralization but the equilibrium constant associated with CO_2 uptake in MEA decreases as the reaction temperature increases.[62,63] As a result, there is a non-monotonic dependence in the
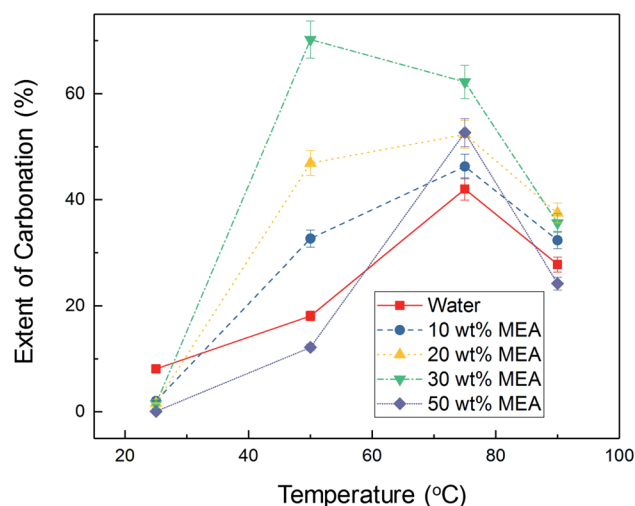

Fig. 2 Extent of carbon mineralization of MgO reacted with water, 10 wt%, 20 wt%, 30 wt%, and 50 wt% at 25 °C, 50 °C, 75 °C, and 90 °C at $P_{CO_2} = 1$ atm for 3 h and stiring rate of 300 rpm. Experiments were performed in duplicate.

combined absorption-mineralization behavior of MgO with temperature.

At similar experimental conditions, 100% conversion of CaO to calcium carbonate was reported.[9] As MEA concentrations are increased starting from DI water to 10 wt% and 20 wt% MEA, high conversions of MgO to magnesium carbonate are achieved at 75 °C. At 30 wt% MEA, higher extents of carbon mineralization were achieved at 50 °C. At 50 wt% MEA, gel formation was
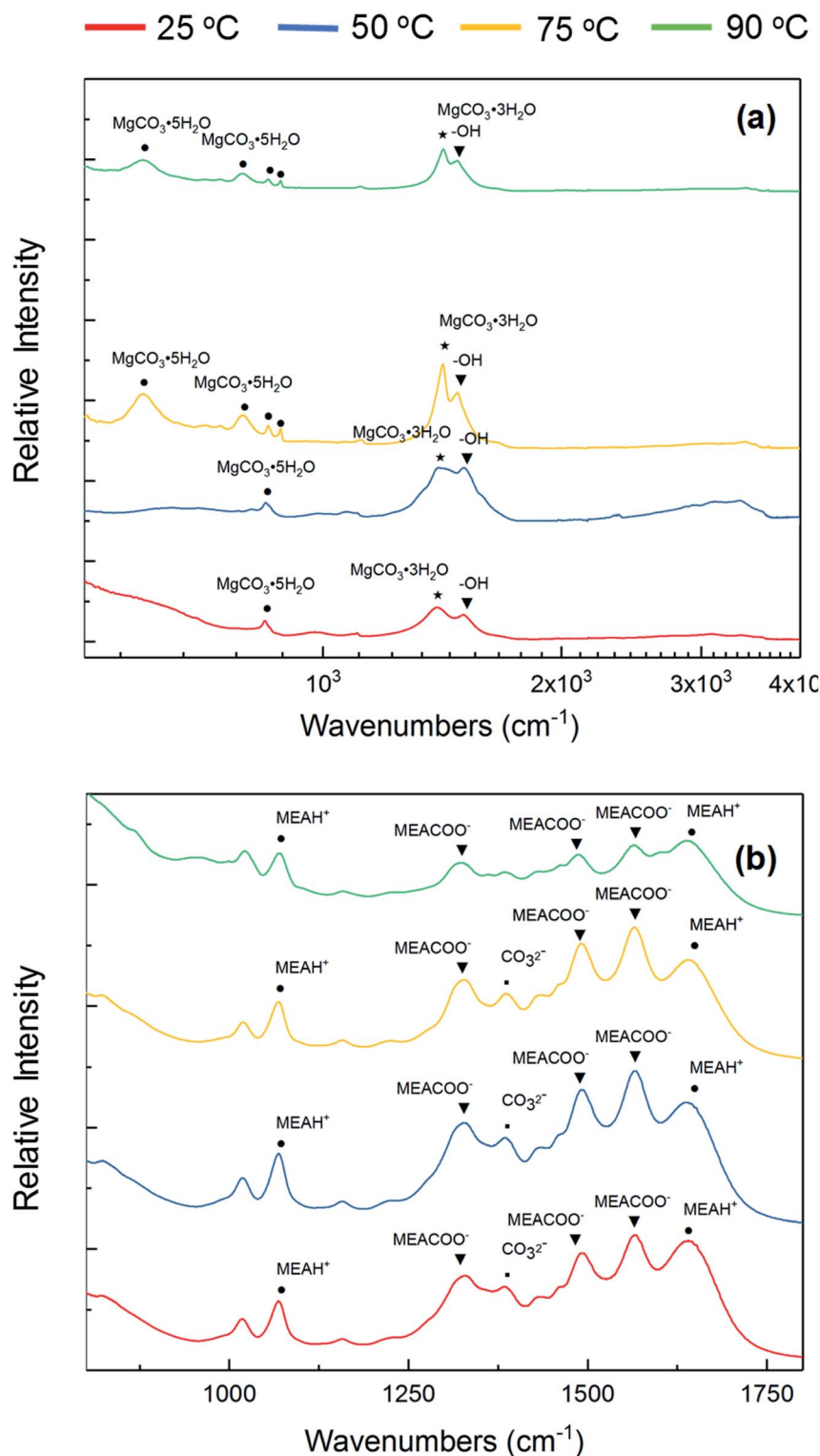
Fig. 3 Identification of the functional groups present in the (a) reacted solid and (b) fluid obtained from reacting MgO with 30 wt% MEA at 50 °C with $P_{CO_2} = 1$ atm for 3 hours and stirring rate of 300 rpm, using ATR-FTIR measurements.

noted with MgO which made it challenging to separate the solid and liquid constituents. Our hypothesis is that the enhanced hydrogen bonding resulting from the interactions between the dissolved fluidic constituents result in gel formation. This observation is consistent with the formation of magnesium carbonate-based porous gels.[64] Our hypothesis for the limited reactivity of MgO at high concentrations of MEA, *i.e.*, 50 wt% emerges from the mass transfer limitations caused by gel formation.

To identify the constituents in the solid phase and aqueous phase, ATR-FTIR analyses were performed. A wide range of phases were identified. Absorption bands at 1471 cm^{-1} and 1515 cm^{-1} indicates ν_3 asymmetric CO_3^{2-} stretching mode, which matches with features of nesquehonite ($MgCO_3 \cdot 3H_2O$), and lansfordite ($MgCO_3 \cdot 5H_2O$).[65–67] The bands at 1097 cm^{-1} and 852 cm^{-1} reflect the ν_1 symmetric C–O, and the ν_2 C–O non-planar bending vibrations, respectively.[65–67] These observations are consistent with previous studies that show the formation of hydrated magnesium carbonates at the experimental conditions of interest (Fig. 3(a) and S1†).[65–67] Analyses of the liquid recovered post-reaction at 30 wt% MEA and 50 °C showed that MEAH$^+$, MEACOO$^-$, and CO_3^{2-} ions are the dominant species present in the aqueous phase (Fig. 3(b) and S2†). At lower MEA concentrations of 10 wt% and 20 wt%, the relative intensities of these liquid species, in particular carbonate species is lower compared to that at 30 wt% MEA. The aqueous species are identified using FT-IR analyses in this study with MgO as the reactant are consistent with the observations reported by Ji and co-workers with CaO as the reactant.[42] The CO_2 uptake and release behavior of MEA is evident from the multiple MEA species detected in the ATR FT-IR spectra.

3.2 Morphological characterization of magnesium carbonates

The morphological features before and after reacting CO_2 with MgO were determined using scanning electron microscopy images. The sizes of the unreacted MgO grains is to the order of a few micrometers (Fig. 4(a)). Needle-shaped nesquehonite ($MgCO_3 \cdot 3H_2O$) is dominant after MgO is reacted with 30 wt% MEA at 50 °C in $pCO_2 = 1$ atm (Fig. 4(b)). Further, *in operando* Ultra Small and Small Angle X-ray Scattering

(USAXS/SAXS) measurements were performed to determine the dynamic evolution in the structural and morphological features as MgO is reacted with CO_2-loaded MEA (Fig. 5(a)). The experimental conditions at which these measurements were performed are 25 °C, 1 atm, and CO_2-loaded MEA concentrations of 30 wt%. These time-resolved measurements show the emergence of carbonate phases in the high q regimes that corresponds to the SAXS regime. The peaks at $q \sim 1.02$ Å^{-1} and $q \sim 0.51$ Å^{-1} correspond to the (0 0 2) and (0 0 1) reflections of lansfordite ($MgCO_3 \cdot 5H_2O$).[68,69] These data suggest that lansfordite growth is a precursor to the formation of nesquehonite.[69] In hydrothermal environments where the effects of temperature and MEA compositions on the accelerated carbon mineralization of MgO to magnesium carbonate are evaluated as shown in Fig. 2, it is hypothesized that lansfordite undergoes pseudomorphic transformations to produce nesquehonite.[69]

Since the characteristic peak for (001) plane of lansfordite ($MgCO_3 \cdot 5H_2O$) emerged after 89 min of reaction time, the data were modeled in two stages.[65–67] In the first stage, the USAXS/SAXS curves were modeled using two unified fit levels in two different q regions, where $q = (4\pi/\lambda)\sin(\theta/2)$ and λ is the wavelength of incident X-ray and θ is the scattering angle.[71,72] The two q-regions 0.001–0.02 Å^{-1} and 0.02–0.8 Å^{-1}, were modeled based on the approach proposed by Beaucage.[73,74] The fit in each level can be described by a Guinier regime and a power-law regime. Typically, the model assumes a spherical and centrosymmetric shape of the scattering objects.[74] However, it can be applied to a broad range of scatterer shapes, including spheres, rods, lamellae, cylinders *etc.* based on its formulation in terms of radius of gyration (R_g) and free power-law slope. In the second stage of fitting, for all the data curves after 89 min, the scattering profiles were fitted using three levels of fits. Like the approach in first stage, two regions of unified fit were modeled in q ranges of 0.001–0.02 Å^{-1} and 0.02–0.3 Å^{-1}, respectively. Additionally, a Lorentzian diffraction peak was fitted in the q range of 0.3–0.8 Å^{-1}. The representative model fits overlaid on experimental data are shown in Fig. S6.† The normalized integrated intensity of (001) peak of lansfordite is presented in Fig. 5(b).[65–67] Additionally, the modeling results from the unified fit in q range of 0.02–0.8 Å^{-1}, were of interest and are discussed further. The power-law slope and radius of gyration (R_g) obtained from the unified fit are presented in Fig. 6(a). The R_g values are representative of pore dimensions.

The evolution in the pore morphology as MgO is converted to $MgCO_3$ is determined by tracking changes in the characteristic radius of gyration, R_g. Initially, an R_g value of ~5 nm was noted for the precursor, MgO. This value is comparable to the representative pore size determined from N_2 BET adsorption measurements (Fig. 6(b1)). The increase in R_g values noted until 61 minutes of reaction time, is attributed to the dissolution of MgO. As discussed earlier, the (001) peak for lansfordite first emerged after 89 minutes of reaction time (Fig. 5(b)), the R_g values started to decrease and achieved a value of ~3.4 nm as the carbonation of MgO began. The changes in the R_g values corresponding to the phase change of MgO to $MgCO_3$ during reaction are mapped in (Fig. 6(b2)). These values of R_g remained
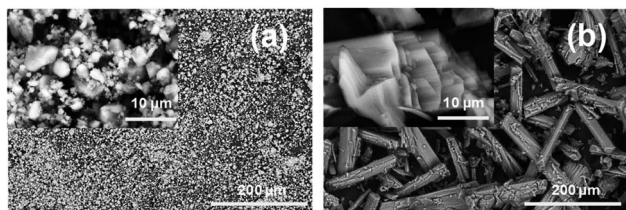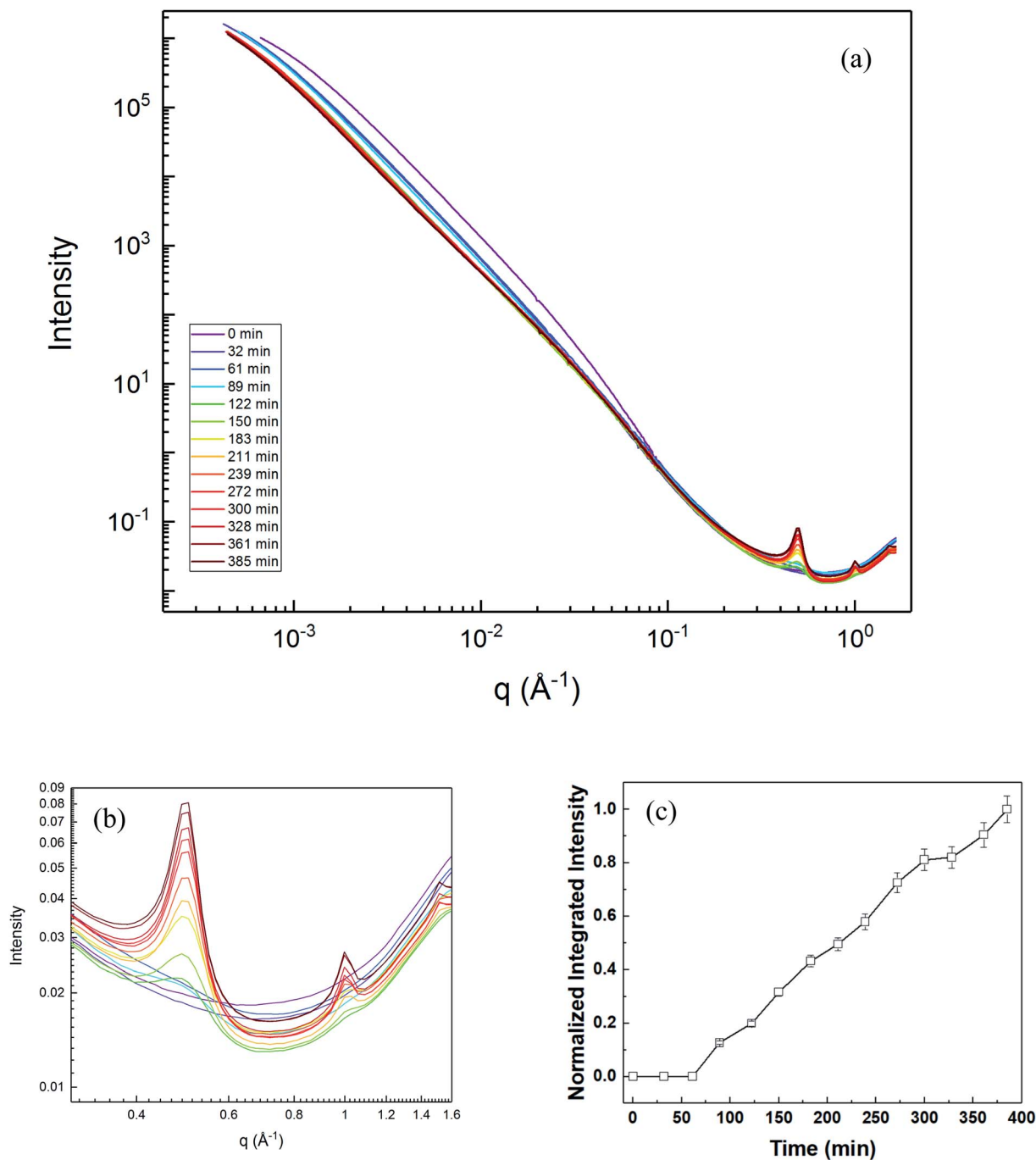

Fig. 4 Comparison of the morphological changes in (a) unreacted magnesium oxide, (b) MgO reacted with 30 wt% MEA and (c) 50 wt% MEA. Experimental conditions for the images shown in (b) and (c) represent 50 °C with $P_{CO_2} = 1$ atm for 3 hours and stirring rate of 300 rpm. The needle-shaped particles in (b) correspond to nesquehonite particles.

Fig. 5 Changes in the combined slit-smeared USAXS/SAXS data as MgO is reacted with CO_2-loaded MEA to produce magnesium carbonate as shown in (a). The characteristic peak of lansfordite at $q = 0.5 \text{ Å}^{-1}$ and the normalized integrated intensity are shown in (b) and (c), respectively. The integrated intensity is normalized to the highest peak intensity which is noted at 385 minutes.

persistent till the end of reaction (385 minutes). For comparison, the pore dimensions of $MgCO_3$ powder obtained after reaction of MgO with 30 wt% MEA in a batch reactor for 3 hours was compared with the R_g value at 183 minutes. The N_2 BET data determined at these experimental conditions and shown in Fig. 6(b3) is mapped to Fig. 6(a). The R_g values determined from USAXS/SAXS measurements are comparable to the pore radius data determined from N_2 BET measurements. The reduction in

the pore radius as carbon mineralization occurs suggests that the diffusion limitations may contribute to the changes in reactivity.

Insights into the evolution of pore-solid interfaces can be obtained from the Porod exponent. Porod exponent between 2 and 3 represents scattering from branched networks or mass fractals.[70] Porod exponents between 2.2–2.8 are noted prior to the development of the lansfordite phase. Concurrent
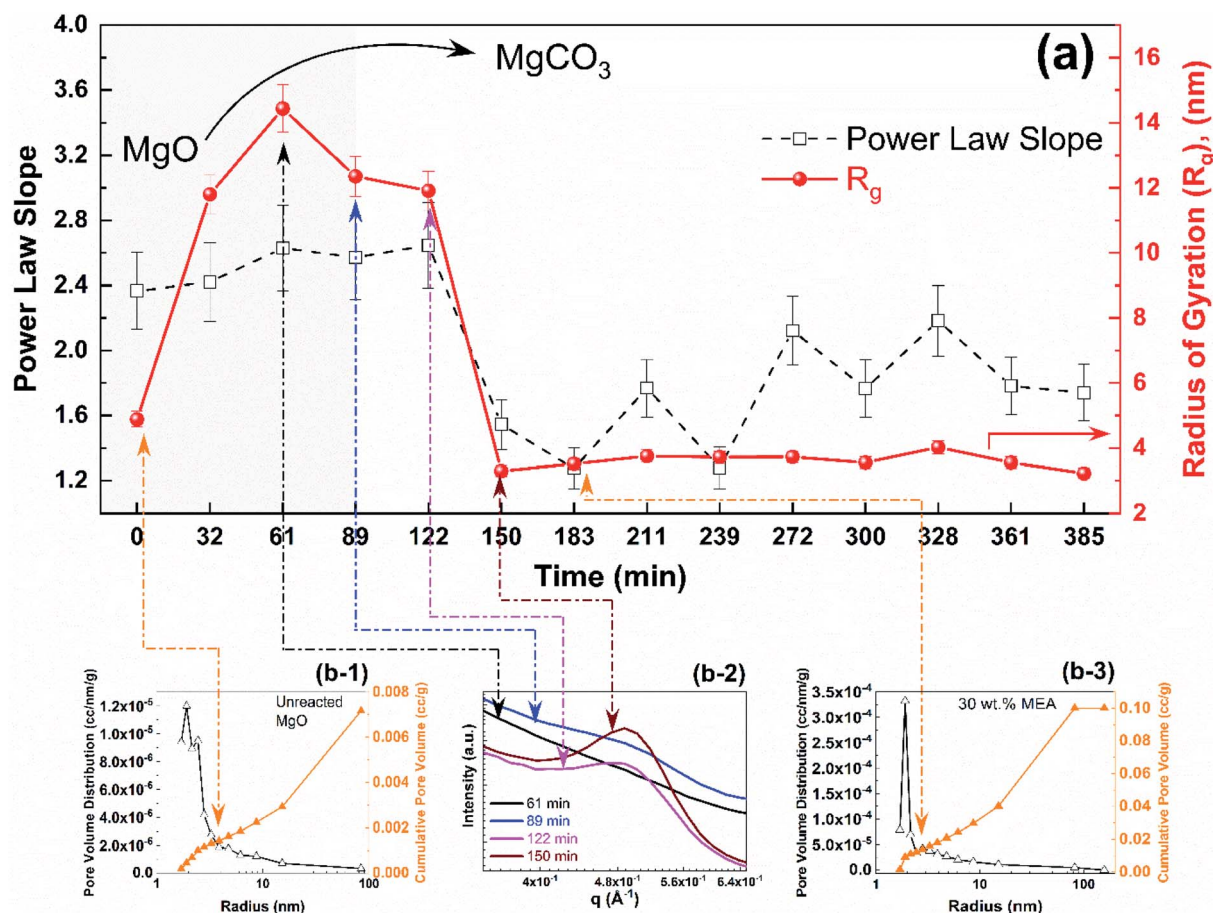
Fig. 6 (a) Power law slope and radius of gyration (R_g) values obtained from the fitting of experimental USAXS/SAXS curves in the q-range of 0.02–0.8 Å^{-1}. The pore size distribution and cumulative pore volume for unreacted MgO and MgO reacted with 30 wt% MEA for 3 hours are represented in (b1) and (b3), respectively. The pore size distributions were determined by using the BJH method on N_2 desorption isotherm. The emergence of (001) lansfordite ($MgCO_3 \cdot 5H_2O$)[68,69] peak from MgO is shown in (b2).

dissolution of MgO and lansfordite phase growth result in Porod slopes in the range of 1.6–2.4. These data show that the fractal character of the pore-solid interfaces evolves as MgO reacts to produce $MgCO_3$. While USAXS/SAXS measurements provide insights into the influence of bulk morphological changes and structural evolution during the carbon mineralization of magnesium oxide, it is challenging to determine the sizes of the magnesium carbonate particles in the proposed process. The research question in this context is as follows: how can we determine the sizes of the carbonate particles once the Mg cations are mobilized in the aqueous phase? To address this research question, we utilize *in operando* Grazing Incidence-Small Angle X-ray Scattering (GI-SAXS) measurements to determine the sizes of the magnesium carbonate particles. Fig. 7(a) is a schematic of the GI-SAXS cell. 0.1988 mL of 30 wt% CO_2-loaded MEA solution was injected into 5 mL 0.1 M $Mg(NO_3)_2$ solution. The reaction vessel used in these experiments was made from silica. To mimic the formation of magnesium carbonate particles on these silica surfaces, we used solid quartz substrate (100). These quartz surfaces were rinsed with acetone to remove any organic contaminants.[75]

Fig. 7(b) is an example of raw 2D GISAXS scattering pattern from quartz (100) substrates with MgO. The original image is shown, without background subtraction and further processing. After background subtraction and 2D data reduction, the reduced data was fitted by Guinier–Porod fit[60] as shown in Fig. 7(c).

The formation of magnesium carbonate particles was noted after about 60 minutes. The scattering curves were obtained by reducing the data contained in the 2-D images.[75] The sizes of the particles are obtained by fitting the Guinier–Porod fit based on eqn (1)–(4).[60] Also, the factor s was set as 1 based on the formation of rod-like shape particles observed in the SEM images in Fig. 4(b). The size distribution in Fig. 7(d) was extrapolated from the Fig. 7(c) based on the maximum entropy method using Irena and Nika packages. From these data, we infer that the sizes of the precipitates are to the order of 15–16 nm (Fig. 7(d)). At these experimental conditions, the formation of hydrated magnesium carbonates is expected.[75] In comparison, the sizes of the calcium carbonate is approximately 2 nm.[75,76] These GI-SAXS data provide insights into the size of the magnesium carbonate particles on silica surfaces, while the
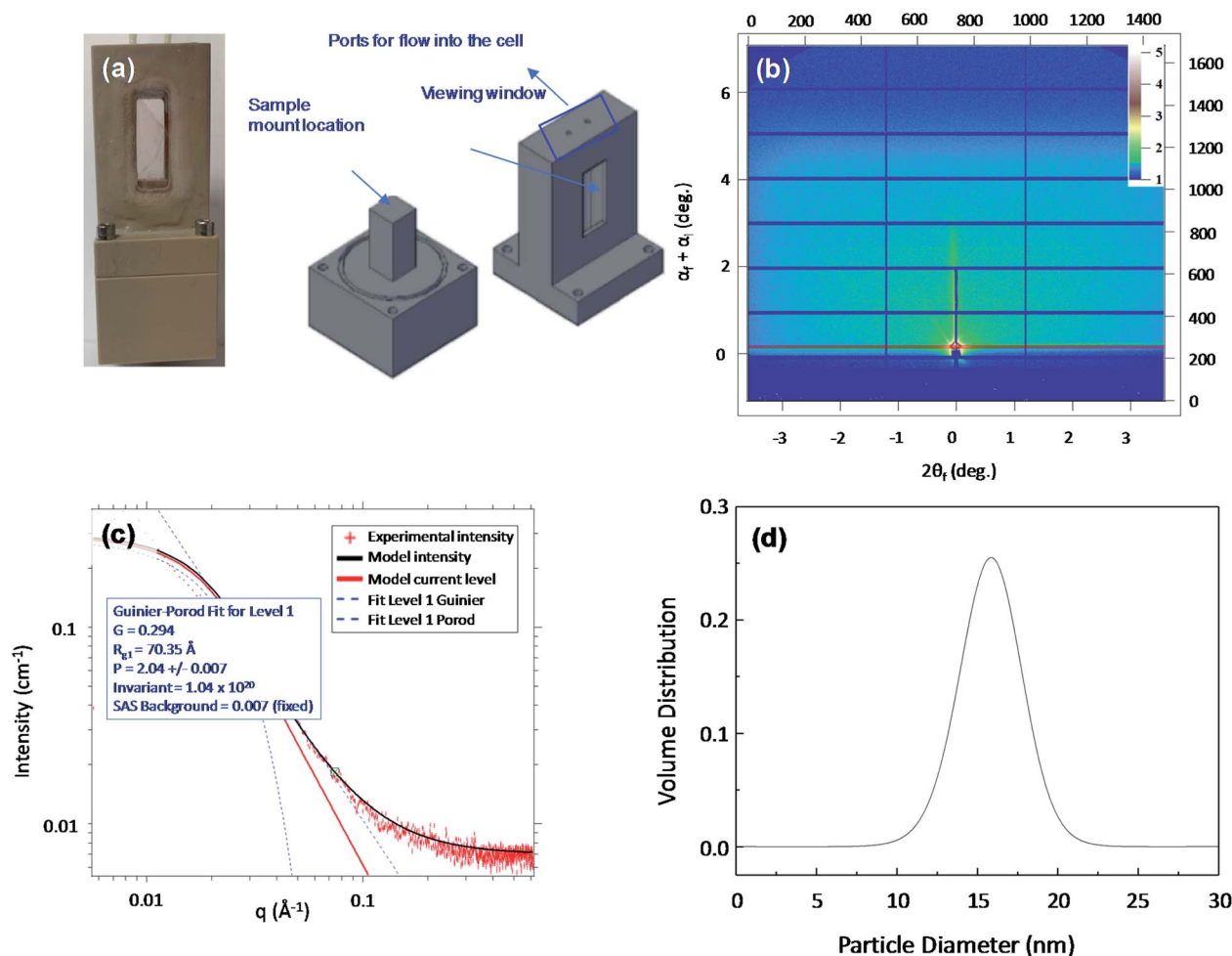
Fig. 7 The *in situ* cell for Grazing Incidence-Small Angle X-ray Scattering (GI-SAXS) measurements is shown in (a). A representative scattering image (b) and the scattering curve (c) that correspond to the nucleation of magnesium carbonate particles on quartz (0 0 1) surface are shown. The size distribution obtained from fitting the scattering curve using the Guinier–Porod slope is shown in (d). The experiments were performed at 25 °C. 0.1988 mL 30 wt% CO_2-loaded MEA solution was injected into 5 mL 0.1 M $Mg(NO_3)_2$ solution, which marked the beginning of the *in situ* measurement.

USAXS/SAXS data show the emergence of metastable lansfordite and the characteristic pore size as MgO is converted to metastable magnesium carbonate phases.

4. Conclusion

In this study, we investigate the effectiveness of utilizing aqueous alkaline amine looping process for the directed synthesis of magnesium carbonate starting from magnesium oxide as the precursor. Experiments were performed in a multiphase reaction environment comprising CO_2 at a pressure of 1 atm with temperature varying between 25 °C to 90 °C, and aqueous concentrations of MEA varying from 0 to 50 wt%. The maximum extent of carbon mineralization achieved with magnesium oxide was 70% in 30 wt% MEA solution at 50 °C for a reaction time of 3 hours. The formation of hydrated phases of magnesium carbonate such as nesquehonite ($MgCO_3 \cdot 3H_2O$) was noted. Small angle X-ray scattering measurements showed the formation of lansfordite at system conditions as likely

precursors prior to the formation of nesquehonite. The high carbonate conversions achieved with the use of magnesium oxide using the aqueous alkaline amine looping demonstrate the effectiveness of using the proposed approach for the direct capture, conversion and storage of CO_2 or can be adapted for the reactive separation of CO_2. In the context of Carbon Capture and Storage (CCS) or more broadly processes needed for decarbonization or carbon removal, we present a single integrated process that combines CO_2 capture and storage as Mg-bearing carbonates. The end-product of this process which is magnesium carbonate produced from anthropogenic CO_2 can be utilized in filler materials. The high extents of carbon mineralization with MgO at significantly lower temperatures of 50 °C demonstrate that the proposed reaction pathways are promising alternatives to the high pressure and high temperature routes or chemically intensive routes for carbon mineralization previously reported in literature. Having demonstrated the feasibility of these chemical pathways with pure precursor MgO, subsequent research efforts will be directed towards

exploring the use of alkaline industrial residues with high Ca and Mg content and naturally occurring Ca- and Mg-bearing silicate minerals for the low temperature and integrated capture, conversion and storage of CO_2 as Ca- and Mg-bearing carbonates.

Conflicts of interest

There are no conflicts to declare.

Acknowledgements

References

1 National Academies of Sciences Engineering and Medicine, *Gaseous Carbon Waste Streams Utilization: Status and Research Needs*, 2019.

2 M. Liu and G. Gadikota, *Energy Fuels*, 2018, **32**, 8193–8201.

3 M. Liu and G. Gadikota, *Fuel*, 2018, **227**, 379–385.

4 S. J. Gerdemann, W. K. O'Connor, D. C. Dahlin, L. R. Penner and H. Rush, *Environ. Sci. Technol.*, 2007, **41**, 2587–2593.

5 K. S. Lackner, D. P. Butt and C. H. Wendt, *Energy Convers. Manage.*, 1997, **38**, S259–S264.

6 K. S. Lackner, Carbonate Chemistry for Sequestering Fossil Carbon, *Annu. Rev. Environ. Resour.*, 2011, **27**, 193–232.

7 A. H. A. Park, R. Jadhav and L. S. Fan, *Can. J. Chem. Eng.*, 2003, **81**, 885–890.

8 A. H. A. Park and L. S. Fan, *Chem. Eng. Sci.*, 2004, **59**, 5241–5247.

9 M. Liu and G. Gadikota, *Energy Fuels*, 2018, **33**, 1722–1733.

10 M. Liu and G. Gadikota, *Geosciences*, 2018, **8**, 445.

11 G. Gadikota, J. Matter, P. Kelemen and A. H. A. Park, *Phys. Chem. Chem. Phys.*, 2014, **10**, 4679–4693.

12 G. Gadikota and A. H. A. Park, *Accelerated Carbonation of Ca- and Mg-Bearing Minerals and Industrial Wastes Using CO_2*, 2014, pp. 115–137.

13 G. Gadikota, K. Fricker, S. H. Jang and A. H. A. Park, in *Advances in CO_2 Capture, Sequestration, and Conversion*, ed. F. Jin, L. N. He and Y. H. Hu, American Chemical Society, 2015, pp. 295–322.

14 G. Gadikota, F. Zhang and A. Allen, *Ind. Eng. Chem. Res.*, 2017, **56**, 11791–11801.

15 G. Gadikota and A. H. A. Park, in *Carbon Dioxide Utilisation*, 2015, pp. 115–137.

16 G. Gadikota, *Geo-chemo-physical studies of carbon mineralization for natural and engineered carbon storage*, Columbia University, 2014.

17 I. M. Power, A. L. Harrison, G. M. Dipple, S. A. Wilson, P. B. Kelemen, M. Hitch and G. Southam, *Rev. Mineral. Geochem.*, 2013, **77**, 305–360.

18 E. R. Bobicki, Q. Liu, Z. Xu and H. Zeng, *Prog. Energy Combust. Sci.*, 2012, **38**, 302–320.

19 M. Salman, Ö. Cizer, Y. Pontikes, R. M. Santos, R. Snellings, L. Vandewalle, B. Blanpain and K. Van Balen, *Chem. Eng. J.*, 2014, **246**, 39–52.

20 D. N. Huntzinger, J. S. Gierke, S. K. Kawatra, T. C. Eisele and L. L. Sutter, *Environ. Sci. Technol.*, 2009, **43**, 1986–1992.

21 V. S. Yadav, M. Prasad, J. Khan, S. S. Amritphale, M. Singh and C. B. Raju, *J. Hazard. Mater.*, 2010, **176**, 1044–1050.

22 A. Sanna, M. Uibu, G. Caramanna, R. Kuusik and M. M. Maroto-Valer, *Chem. Soc. Rev.*, 2014, **43**, 8049–8080.

23 J. Fagerlund and R. Zevenhoven, *Int. J. Greenhouse Gas Control*, 2011, **5**, 1406–1412.

24 S. Eloneva, P. Mannisto, A. Said, C. J. Fogelholm and R. Zevenhoven, *Greenhouse Gases: Sci. Technol.*, 2011, **1**, 305–311.

25 Z. Duan and R. Sun, *Chem. Geol.*, 2003, **193**, 257–271.

26 Z. Duan, R. Sun, C. Zhu and I. M. Chou, *Mar. Chem.*, 2006, **98**, 131–139.

27 Y. Chen and S. L. Brantley, *Chem. Geol.*, 2000, **165**, 267–281.

28 R. A. Wogelius and J. V. Walther, *Chem. Geol.*, 1992, **97**, 101–112.

29 A. Awad, A. F. Koster Van Groos and S. Guggenheim, *Geochim. Cosmochim. Acta*, 2000, **10**, 1765–1772.

30 Y. Liu, A. A. Olsen and J. D. Rimstidt, *Am. Mineral.*, 2006, **91**, 455–458.

31 M. Hänchen, S. Krevor, M. Mazzotti and K. S. Lackner, *Chem. Eng. Sci.*, 2007, **22**, 6412–6422.

32 A. J. Ellis, *Am. J. Sci.*, 2010, **257**, 354–365.

33 M. Werner, S. Hariharan and M. Mazzotti, *Phys. Chem. Chem. Phys.*, 2014, **16**, 24978–24993.

34 W. White, *Acta Carsol.*, 2016, **44**(3), 349–362.

35 M. Vinoba, D. H. Kim, K. S. Lim, S. K. Jeong, S. W. Lee and M. Alagar, *Energy Fuels*, 2011, **115**, 20209–20216.

36 I. M. Power, A. L. Harrison and G. M. Dipple, *Environ. Sci. Technol.*, 2016, **50**, 2610–2618.

37 P. C. Sahoo, Y. N. Jang and S. W. Lee, *J. Cryst. Growth*, 2013, **373**, 96–101.

38 H. Zhao, Y. Park, D. H. Lee and A. H. A. Park, *Phys. Chem. Chem. Phys.*, 2013, **36**, 15185–15192.

39 W. Xue, X. Liu, X. Zheng and C. Ding, *Surf. Coat. Technol.*, 2005, **200**, 2420–2427.

40 M. M. Reddy and W. D. Gaillard, *J. Colloid Interface Sci.*, 1981, **80**, 171–178.

41 P. Bénézeth, G. D. Saldi, J. L. Dandurand and J. Schott, *Chem. Geol.*, 2011, **286**, 21–31.

42 L. Ji, H. Yu, K. Li, B. Yu, M. Grigore, Q. Yang, X. Wang, Z. Chen, M. Zeng and S. Zhao, *Appl. Energy*, 2018, **225**, 356–366.

43 M. Arti, M. H. Youn, K. T. Park, H. J. Kim, Y. E. Kim and S. K. Jeong, *Energy Fuels*, 2017, **31**, 763–769.

44 Q. Li, S. Gupta, L. Tang, S. Quinn, V. Atakan and R. E. Riman, *Frontiers in Energy Research*, 2016, **3**, 53.

45 R. E. Riman and Q. Li, *US. Pat.*, 13/008, 464, 2011.

46 M. A. Shand, *The Chemistry and Technology of Magnesia*, 2006.

47 P. Falkowski, R. J. Scholes, E. Boyle, J. Canadell, D. Canfield, J. Elser, N. Gruber, K. Hibbard, P. Hogberg, S. Linder, F. T. Mackenzie, B. Moore, T. Pedersen, Y. Rosental, S. Seitzinger, V. Smetacek and W. Steffen, *Science*, 2000, **290**, 291–296.

48 J. Ilavsky, P. R. Jemian, A. J. Allen, F. Zhang, L. E. Levine and G. G. Long, *J. Appl. Crystallogr.*, 2009, **42**, 469–479.

49 J. Ilavsky, F. Zhang, A. J. Allen, L. E. Levine, P. R. Jemian and G. G. Long, *Metall. Mater. Trans. A*, 2013, **44**, 68–76.

50 A. Benedetti, J. Ilavsky, C. Segre and M. Strumendo, *Chem. Eng. J.*, 2019, **355**, 760–776.

51 J. Ilavsky, F. Zhang, R. N. Andrews, I. Kuzmenko, P. R. Jemian, L. E. Levine and A. J. Allen, *J. Appl. Crystallogr.*, 2018, **51**, 867–882.

52 E. J. Swanson, K. J. Fricker, M. Sun and A. H. A. Park, *Phys. Chem. Chem. Phys.*, 2014, **42**, 23440–23450.

53 G. Gadikota, E. Swanson, H. Zhao and A. H. A. Park, *Ind. Eng. Chem. Res.*, 2014, **53**, 6664–6676.

54 S. J. Gerdemann, W. K. O'Connor, D. C. Dahlin, L. R. Penner and H. Rush, *Environ. Sci. Technol.*, 2007, **41**, 2587–2593.

55 G. Gadikota, F. Zhang and A. J. Allen, *Fuel*, 2017, **196**, 195–209.

56 D. R. Black, D. Windover, A. Henins, D. Gil, J. Filliben and J. P. Cline, *Powder Diffr.*, 2010, **25**, 187–190.

57 J. Ilavsky and P. R. Jemian, *J. Appl. Crystallogr.*, 2009, **42**, 347–353.

58 J. Ilavsky, *J. Appl. Crystallogr.*, 2012, **45**, 324–326.

59 S. Frykstrand, J. Forsgren, A. Mihranyan and M. Strømme, *Microporous Mesoporous Mater.*, 2014, **190**, 99–104.

60 B. Hammouda, *J. Appl. Crystallogr.*, 2010, **43**, 716–719.

61 Y. E. Kim, J. A. Lim, S. K. Jeong, Y. Il Yoon, S. T. Bae and S. C. Nam, *Bull. Korean Chem. Soc.*, 783–787.

62 M. Gupta, E. F. Da Silva, A. Hartono and H. F. Svendsen, *J. Phys. Chem. B*, **116**, 1865–1875.

63 I. Kim and H. F. Svendsen, *Ind. Eng. Chem. Res.*, **46**, 5803–5809.

64 S. Frykstrand, J. Forsgren, A. Mihranyan and M. Strømme, *Microporous Mesoporous Mater.*, 2014, **190**, 99–104.

65 B. Morgan, S. A. Wilson, I. C. Madsen, Y. M. Gozukara and J. Habsuda, *Int. J. Greenhouse Gas Control*, 2015, **39**, 366–376.

66 W. Yin, Y. Wang, Q. Ji, J. Yao, Y. Hou, L. Wang and W. Zhong, *Int. J. Miner., Metall. Mater.*, 2014, **21**, 304–310.

67 L. Hopkinson, P. Kristova, K. Rutt and G. Cressey, *Geochim. Cosmochim. Acta*, 2012, **76**, 1–13.

68 G. Giester, C. L. Lengauer and B. Rieck, *Mineral. Petrol.*, 2000, **70**, 153–163.

69 D. W. Ming and W. T. Franklin, *Soil Sci. Soc. Am. J.*, 2010, **49**, 1303–1308.

70 D. W. Schaefer and K. D. Keefer, *Phys. Rev. Lett.*, 1986, **56**, 2199.

71 O. Glatter and O. Kratky, *Small Angle X-ray Scattering*, Academic Press, 1982, vol. 18, pp. 1–19.

72 A. Guinier and G. Fournet, *Small-Angle Scattering of X-rays*, John Wiley and Sons, New York, 1955.

73 G. Beaucage, *J. Appl. Crystallogr.*, 1995, **28**, 717–728.

74 G. Giester, C. L. Lengauer and B. Rieck, *Mineral. Petrol.*, 2000, **70**, 153–163.

75 A. Fernandez-Martinez, Y. Hu, B. Lee, Y. S. Jun and G. A. Waychunas, *Environ. Sci. Technol.*, 2013, **47**, 102–109.

76 A. V. Radha, A. Fernandez-Martinez, Y. Hu, Y.-S. Jun, G. A. Waychunas and A. Navrotsky, *Geochim. Cosmochim. Acta*, 2012, **90**, 83–95.